

# Invited Feature Article

## Perforated, Freely Suspended Layer-by-Layer Nanoscale Membranes

Dmitry Zimnitsky,<sup>†</sup> Valeriy V. Shevchenko,<sup>‡</sup> and Vladimir V. Tsukruk<sup>\*,†</sup>

*Georgia Institute of Technology, School of Materials Science and Engineering, Atlanta, Georgia 30332, and National Academy of Sciences of Ukraine, Institute of Macromolecular Chemistry, Kiev, 02160 Ukraine*

Received December 10, 2007. Revised Manuscript Received February 8, 2008

Ultrathin, perforated, and freely suspended membranes with uniform nanopores in the range of tens of nanometers have been fabricated using a fast, simple method of spin-assisted layer-by-layer assembly on hydrophobic substrates. Membranes with thicknesses down to 20 nm were robust enough to be released from the sacrificial substrates, transferred onto various surfaces, and suspended over microscopic openings. The nanopore size can be controlled by tuning the number of polyelectrolyte bilayers, spinning speed, and a proper selection of hydrophobic substrates. We demonstrate that the formation of nanopores is caused by the partial dewetting of polyelectrolyte layers in the course of their deposition on the underlying hydrophobic surfaces. The nanoscale thickness of perforated membranes with relatively uniform size and a high concentration of nanopores provides perspectives for higher rates of transport through freely suspended LbL membranes. The highly perforated LbL membranes introduced here can serve as a novel platform for ultrafine separation considering an intriguing combination of nanopores, nanoscale membrane thickness, and easy functionalization.

### Introduction

**Nanoporous Membranes.** Synthetic membranes with pore sizes approaching molecular dimensions are considered to be critical for certain prospective applications in membrane science and technology.<sup>1–4</sup> The development of such membranes is inspired by the fact that selective transport through biological membranes is enabled by supramolecular assemblies with responsive and nanoscopic pore sizes.<sup>5,6</sup> Many scientifically interesting, technically challenging, and commercially attractive separation problems cannot be solved with existing synthetic membranes. There is a need of novel membranes with high selectivity, uniform pore distribution, and high flux for separation of various objects (e.g. isomers, enantiomers, nanoparticles, and biomolecules).

The recent developments of polymer-based membranes having advanced functions in various separation processes have been comprehensively reviewed by Ulbricht. (See Figure 1 for various membrane designs.<sup>7</sup>) The general strategies employed for the design of high-performance porous membranes include a narrow

pore size distribution, high porosity, and minimal tortuosity (ideally straight, vertically aligned pores though the barrier). Additional functionalities for selective interactions (based on charge, molecular recognition, or catalysis) would greatly improve the selectivity of the membranes. Minimizing the thickness of the membrane barrier layer is also essential for ultrafiltration applications. Preferably, the thickness of the porous media should be comparable to the size of the pores to increase the rate of transport greatly.

Existing ultrafiltration membranes suffer from several common issues that are directly related to the way in which they are fabricated. Several examples of nanofabricated membranes are the track membranes<sup>8,9</sup> (10 μm thickness combined with 20–50 nm diameter pores) and polymer membranes with impregnated gold nanotubes<sup>10</sup> (6 μm thickness, 2–5 nm pore size). They usually possess a broad pore size distribution and are many orders of magnitude thicker than the molecules that they are designed to separate (typical pore sizes within 10–100 nm with a common thickness of several micrometers) (Figure 1). This leads to poor size cutoff properties, trapping or adsorption of particles and large molecules within the membranes,<sup>11</sup> filtrate loss within the membranes, and low transport rates.<sup>12,13</sup> A combination of broad pore size distribution, the random open/close character of pores, and the low relative concentration of through pores (within (1–10) × 10<sup>8</sup> pores/cm<sup>2</sup>) limits the rate of flux through the membranes. Nanofabricated membranes have great potential in molecular separation applications by offering more precise structural control and more uniform separation,<sup>14,15</sup> yet the overall transport is still

\* E-mail: vladimir@mse.gatech.edu.

<sup>†</sup> Georgia Institute of Technology.

<sup>‡</sup> National Academy of Sciences of Ukraine.

- (1) Nishizawa, M.; Menon, V. P.; Martin, C. R. *Science* **1995**, 268, 700.
- (2) Hotnung, M. *Science* **1995**, 267, 473.
- (3) Beck, J. S.; Vartuli, J. C.; Roth, W. J.; Leonowicz, M. E.; Kresge, C. T.; Schmitt, K. D.; Chu, C. T.-W.; Olson, D. H.; Sheppard, E. W.; McCullen, S. B.; Higgins, J. B.; Schlenkert, J. L. *J. Am. Chem. Soc.* **1992**, 114, 10834.
- (4) Dujardin, E.; Ebbesen, T. W.; Hiura, H.; Tanigaki, K. *Science* **1994**, 265, 1850.

- (5) (a) Sukharev, S.; Betanzos, M.; Chiang, C.-S.; Guy, H. R. *Nature* **2001**, 409, 720. (b) Perozo, E.; Cortes, D. M.; Sompornspitup, K. A.; Martinac, B. *Nature* **2002**, 418, 942.

- (6) Ornatska, M.; Jones, S.; Naik, R.; Stone, M.; Tsukruk, V. V. *J. Am. Chem. Soc.* **2003**, 125, 12722.

- (7) Ulbricht, M. *Polymer* **2006**, 47, 2217.

- (8) Shtanko, N. I.; Kabanov, V. Ya.; Apel, P. Yu.; Yoshida, M.; Vilenskii, A. I. *J. Membr. Sci.* **2000**, 179, 155.

- (9) Kravets, L. I.; Dmitriev, S. N.; Sleptsov, V. V.; Elinson, V. M. *Surf. Coat. Technol.* **2003**, 174, 821.

- (10) Jirage, K. B.; Hulteen, J. C.; Martin, C. R. *Science* **1997**, 268, 655.

(11) Pusch, W.; Walch, A. *Angew. Chem., Int. Ed. Engl.* **1982**, 21, 660.

(12) Tong, H. D.; Jansen, H. V.; Gadgil, V. J.; Bostan, C. G.; Berenschot, E. van.; Rijn, C. J. M.; Elwenspoek, M. *Nano Lett.* **2004**, 4, 283.

(13) Kuiper, S.; van Rijn, C. J. M.; Nijdam, W.; Elwenspoek, M. C. *J. Membr. Sci.* **1998**, 150, 1.

(14) Yamaguchi, A.; Uejio, F.; Yoda, T.; Uchida, T.; Tanamura, Y.; Yamashita, T.; Teramae, N. *Nat. Mater.* **2004**, 3, 337.

(15) Lee, S. B.; Martin, C. R. *J. Am. Chem. Soc.* **2002**, 124, 11850.

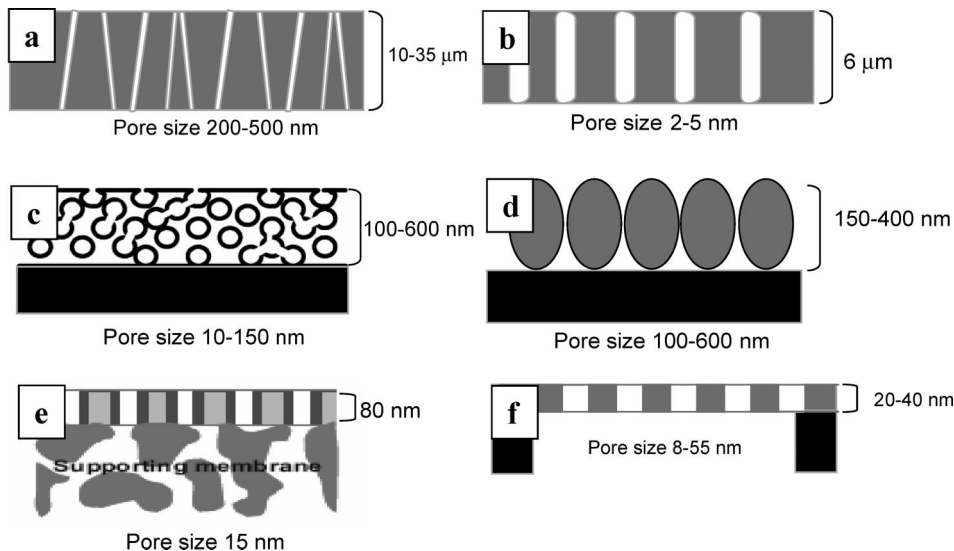


**Figure 1.** General schematics of track membranes<sup>8,9</sup> (a), membranes with gold tubules<sup>10</sup> (b), LbL porous films<sup>47</sup> (c), cross-linked hydrogel films<sup>19</sup> (d), block-copolymer membranes<sup>24</sup> (e), cross-linked polyisoprene membranes,<sup>25</sup> annealed silicon membranes,<sup>27</sup> and LbL membranes reported in this work (f).

limited by their micrometer-scale thicknesses.<sup>16</sup> The reduced membrane thickness combined with the straight, cylindrical pore shape is considered to be critical for the dramatic increase in membrane flux due to the greatly reduced diffusion time across the membrane.

The preparation of a defect-free selective membrane with a thickness below 50 nm using conventional fabrication methods is fundamentally difficult.<sup>17</sup> Several attempts have been made using Langmuir–Blodgett (LB) monolayers of functional amphiphilic molecules as ultrathin selective barriers. However, stable and defect-free composite LB membranes capable of sustaining stresses associated with transfer to the freely suspended state were not obtained consistently. Also, the fabrication of LB multilayers did not yield the expected membrane performance that would justify the very large efforts.<sup>18</sup> Alternatively, cross-linkable hydrogel films have been employed as responsive porous materials. Recently, Minko and co-workers fabricated films of poly(2-vinylpyridine) seated on the supporting silicon substrate with two-dimensionally arranged submicrometer pores.<sup>19</sup> Pore formation occurred during deposition and required a humid environment. Cross-linking the films made them insoluble (stable) in organic solvents and acidic water. The pore size of these cross-linked films was in the range of hundreds of nanometers, which was dependent upon the pH of the solution.

The assembly of block copolymers into periodic microphase structures with well-defined microdomains of a few to tens of nanometers across has been extensively studied from the perspective of their potential to provide nanoporous structures.<sup>20–22</sup> Arrays of nanopores with diameters of 6 to 32 nm were produced by the selective removal of the poly(methyl

methacrylate) (PMMA) homopolymer from spin-cast films of PS-PMMA block-copolymer polystyrene.<sup>23</sup> In another example, Russell and co-workers prepared double-layer nanoporous membranes suitable for virus filtration.<sup>24</sup> The film was 80 nm thick and had 15-nm-diameter cylindrical nanopores with a very narrow pore size distribution, which is a signature of block-copolymer materials. In spite of the low thickness and precise control of pore size, block-copolymer films were not robust enough to maintain their integrity in a freely suspended state. Thus, conventional microfiltration porous membrane was needed to support these ultrathin nanoporous films, negating their nanoscale thickness and prospective high transport rate (Figure 1).

Most of the nanoporous films described above are supported by the underlying substrate and are not strong enough to be released from the substrate while preserving their integrity in the unsupported state (freely suspended across microscopic openings). Truly freely suspended membranes with 40 nm thickness and 55 nm through nanopores have been prepared via an LB routine.<sup>25,26</sup> Hydrophobized silica colloids and polyisoprene have been mixed and spread onto a water surface to form a hybrid monolayer in which 2D ordered domains of submicrometer particles were embedded in a polymer monolayer matrix. Photochemical cross-linking of the polyisoprene, followed by transfer to a gold grid with 100 μm openings, yielded freely suspended membranes. Dissolving the colloidal particles gives rise to uniform nanopores. However, pores with dimensions below 50 nm could not be achieved using this approach, and their concentration should be kept low to avoid the disintegration of the film.

Among inorganic membranes, ultrathin freely suspended perforated silicon membranes with pore sizes below 50 nm and membrane thickness comparable to the size of pores have been demonstrated recently.<sup>27</sup> Nanoscopic voids were formed spontaneously as nanocrystals nucleated and grew in a 15-nm-thick amorphous silicon film during rapid thermal annealing. The voids

(16) Martin, F.; Walczak, R.; Bojarski, A.; Cohen, M.; West, T.; Cosentino, C.; Ferrari, M. *J. Controlled Release* **2005**, *102*, 123.

(17) Bruening, M. L.; Sullivan, D. M. *Chem.–Eur. J.* **2002**, *8*, 3833.

(18) Penacorada, F.; Angelova, A.; Kamusewitz, H.; Reiche, J.; Brehmer, L. *Langmuir* **1995**, *11*, 612.

(19) Orlov, M.; Tokarev, I.; Scholl, A.; Doran, A.; Minko, S. *Macromolecules* **2007**, *40*, 2086.

(20) Park, M.; Harrison, C. K.; Chaikin, M.; Register, R. A.; Adamson, D. H. *Science* **1997**, *276*, 1407.

(21) Thurn-Albrecht, T.; Schotter, J.; Kästle, A.; Emley, N.; Shibauchi, T.; Krusin-Elbaum, L.; Guarini, K.; Black, C. T.; Tuominen, M. T.; Russell, T. P. *Science* **2000**, *290*, 2126.

(22) Black, C. T.; Guarini, K. W.; Milkove, K. R.; Baker, S. M.; Tuominen, M. T.; Russell, T. P. *Appl. Phys. Lett.* **2001**, *79*, 409.

(23) Jeong, U.; Ryu, D. Y.; Kim, J. K. *Macromolecules* **2003**, *36*, 10126.

(24) Yang, S. Y.; Ryu, I.; Kim, H. Y.; Kim, J. K.; Jang, S. K.; Russell, T. P. *Adv. Mater.* **2006**, *18*, 709.

(25) Xu, H.; Goedel, W. A. *Langmuir* **2002**, *18*, 2363.

(26) Xu, H.; Goedel, W. A. *Angew. Chem., Int. Ed.* **2003**, *42*, 4694.

(27) Striemer, C. C.; Gaborski, T. R.; McGrath, J. L.; Fauchet, P. M. *Nature* **2007**, *445*, 749.

span the membrane to create nanopores. These silicon membranes, however, were prepared using a highly sophisticated and expensive approach, and the distribution of pore sizes was rather broad.

**Layer-by-Layer Assembly of Nanoporous Materials.** An alternative approach to the formation of nanoporous membranes utilizes the layer-by-layer (LbL) assembly of polyelectrolytes (Figure 1).<sup>28,29</sup> There is much potential in the use of LbL multilayer films as separation membranes because building principles enable a very small total thickness of the multilayered films.<sup>7,30–33</sup> Versatility and easy fabrication of functionalized membranes with controlled porosity and nanoscale thickness made LbL nanoporous membranes a promising class despite significant technological issues that remain before any practical applications can be made. Recent advances in the fabrication of robust, flexible, and freely suspended LbL membranes open the way for designing similar but highly perforated membranes capable of sustaining high stresses.<sup>34</sup>

In recent studies, Rubner and co-workers<sup>35–38</sup> discovered that microporous and nanoporous multilayered films can be formed by immersing poly(acrylic acid)/poly(allylamine) (PAA-PAH) LbL films in acidic solution (pH 2.4). The resulting films may undergo a secondary reorganization in neutral water, leading to morphology with more discrete through pores. The transition of PAA-PAH multilayers to the porous state can be completely and repeatedly reversed by treatment with different solutions. To lock the porous morphology, it is necessary to heat the film to high temperature to form a cross-linked structure with the amidization reaction between  $\text{COO}^-$  groups in PAA and  $\text{NH}_3^+$  groups in PAH.

Similarly, Zhang and co-workers reported that the hydrogen-bonded LbL assembly of films composed of PAA/poly(4-vinylpiridine) (PAA/P4VP) multilayers have been used to fabricate microporous LbL films after post-treatment in basic aqueous solution at different temperatures.<sup>39–43</sup> In another study, Jin and co-workers prepared microporous poly(diallyldimethylammonium chloride)/poly(sodium 4-styrenesulfonate) (PDDA/PSS) multilayered films by treating the original LbL films with hot water.<sup>44,45</sup> Exposing the PAA/PAH multilayers deposited from salt-containing polyelectrolyte solution to pure water can also result in the formation of nanoporous multilayered films.<sup>46</sup>

- (28) *Protein Architecture: Interfacial Molecular Assembly and Immobilization Biotechnology*; Lvov, Y., Möhwald, H., Eds.; Marcel Dekker: New York, 2000.
- (29) Tsukruk, V. V. *Prog. Polym. Sci.* **1997**, 22, 247.
- (30) *Multilayer Thin Films*; Decher, G. Schlenoff, J. B., Eds.; Wiley-VCH: Weinheim, Germany, 2003.
- (31) Lvov, Y.; Decher, G.; Möhwald, H. *Langmuir* **1993**, 9, 481.
- (32) Decher, G. *Science* **1997**, 277, 1232.
- (33) Tang, Z.; Kotov, N. A.; Magonov, S.; Ozturk, B. *Nat. Mater.* **2003**, 2, 413.
- (34) Jiang, C.; Markutsya, S.; Pikus, Y.; Tsukruk, V. V. *Nat. Mater.* **2004**, 3, 721.
- (35) Mendelsohn, J. D.; Barrett, C. J.; Chan, V. V.; Pal, A. J.; Mayes, A. M.; Rubner, M. F. *Langmuir* **2000**, 16, 5017.
- (36) Hiller, J.; Mendelsohn, J. D.; Rubner, M. F. *Nat. Mater.* **2002**, 1, 59.
- (37) Zhai, L.; Nolte, A. D.; Cohen, R. E.; Rubner, M. F. *Macromolecules* **2004**, 37, 6113.
- (38) Berg, M. C.; Zhai, L.; Cohen, R. E.; Rubner, M. F. *Biomacromolecules* **2006**, 7, 357.
- (39) Fu, Y.; Bai, S. L.; Cui, S. X.; Qiu, D. L.; Wang, Z. Q.; Zhang, X. *Macromolecules* **2002**, 35, 9451.
- (40) Zhang, H. Y.; Fu, F.; Wang, D.; Wang, L. Y.; Wang, Z. Q.; Zhang, X. *Langmuir* **2003**, 19, 8497.
- (41) Bai, S. L.; Wang, Z. Q.; Zhang, X. *Langmuir* **2004**, 20, 11828.
- (42) Bai, S. L.; Wang, Z. Q.; Gao, J.; Zhang, X. *Eur. Polym. J.* **2006**, 42, 900.
- (43) Zhang, H.; Wang, D.; Wang, Z.; Zhang, X. *Eur. Polym. J.* **2007**, 43, 2784.
- (44) Qin, S.; Chen, L. S.; Shi, Y.; Liao, Q.; Jin, X. G. *Chem. J. Chin. Univ.* **2005**, 26, 1183.
- (45) Qin, S.; Wei, D. S.; Liao, Q.; Jin, X. G. *Macromol. Rapid Commun.* **2006**, 27, 11.
- (46) Fery, A.; Schöler, B.; Cassagneau, T.; Caruso, F. *Langmuir* **2001**, 17, 3779.

It is suggested that the formation of nanoporous films occurs by the breakage of the interchain ionic bonds and rearrangement of the polyelectrolyte backbones inside the films, triggered by the variation of the pH, temperature, or ionic strength.

Caruso and co-workers reported another strategy for the fabrication of nanoporous LbL films.<sup>47</sup> The authors employed a removable polyelectrolyte template composed of PAA and a blend of PAH and a hydrogen-bonding P4VP. This film was cross-linked, and the P4VP was removed by immersing into a basic solution (pH 10) to obtain nanoporous films with 10–50 nm pores. Alternatively, silica nanoparticles have been included in polyelectrolyte bilayers composed of PAA and PAH.<sup>48</sup> Porous supported films were formed by the chemical cross-linking of these films, followed by the removal of the particles. In another study, it was demonstrated that the alternate deposition of exponentially and linearly growing polyelectrolyte multilayers may lead to the formation of multicompartiment films.<sup>49</sup> The nanometer-sized multilayer barriers deposited on or between compartments were designed to respond to mechanical stimuli acting as nanovalves.

It is worth noting that in all cases cited above porous LbL films were fabricated onto solid substrates. One of the few exceptions of a freely suspended porous LbL film was designed for the potential selective ion and gas separation.<sup>50</sup> Titania nanoshells were assembled with PAA to produce coatings with a network of voids and channels in the film. The thickness of a stable film ranged from 200 to 400 nm, and the diameter of the channels was on the order of 0.3–1 nm.

Nanoporous LbL membranes possessed a porous but nonperforated structure in most cases (i.e. the pores were not truly through holes). Another issue is the insufficient strength of the LbL films for transfer to the freely suspended state. For instance, to fabricate freely suspended perforated membranes the authors in ref 49 had to increase the thickness of membranes (micrometers) dramatically and obtained only submicrometer and micrometer size pores. Thus, in spite of numerous studies, the facile preparation of robust freely suspended LbL membranes with nanoscale thickness and uniform nanopores remains a great challenge.

In this study, ultrathin (thickness down to 20 nm), perforated, LbL membranes with through nanopores with a diameter below 50 nm were fabricated using the fast, simple routine of spin-assisted LbL assembly on smooth, hydrophobic sacrificial substrates. The perforated LbL films fabricated here are robust enough to be freely suspended over microscopic (up to 100  $\mu\text{m}$  across) openings. The underlying hydrophobic sacrificial substrates promoted the formation of nanovoids in the LbL films in the course of their formation as a result of the partial dewetting of polyelectrolyte layers. The size of the nearly cylindrical nanopores is controlled by varying the number of polyelectrolyte bilayers and parameters of spin-assisted LbL assembly.

## Experimental Section

**Materials.** The polyelectrolytes, poly(allylamine hydrochloride) (PAH, MW = 70 000), and poly(sodium 4-styrenesulfonate) (PSS, MW = 70 000) were purchased from Aldrich and used without further purification. Polyvinyl acetate (PVA, MW = 50 000), polyhydroxystyrene (PHS, MW = 8000), poly(methyl metacrylate) (PMMA, MW = 120 000), and polystyrene (PS, MW 250 000) were purchased from Aldrich and used as underlying sacrificial substrates

(47) Li, Q.; Quinn, J. F.; Caruso, F. *Adv. Mater.* **2005**, 17, 2058.

(48) Li, Q.; Quinn, J. F.; Wang, Y.; Caruso, F. *Chem. Mater.* **2006**, 18, 5480.

(49) Mertz, D.; Hemmerle, J.; Mutterer, J.; Olliver, S.; Voegel, J.-C.; Schaff, P.; Lavalle, P. *Nano Lett.* **2007**, 7, 657.

(50) Koktysh, D. S.; Liang, X.; Yun, B.-G.; Pastoriza-Santos, I.; Matts, R.; Giersig, M.; Serra-Rodríguez, C.; Liz-Marzan, L.; Kotov, N. A. *Adv. Funct. Mater.* **2002**, 12, 255.

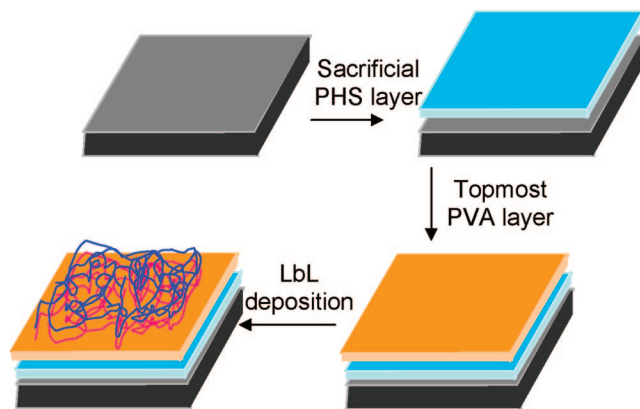


**Figure 2.** General scheme for the deposition of PHS sacrificial and topmost hydrophobic PVA films for the fabrication of perforated LbL films.

for the deposition of LbL films. Nanopure water with a resistivity of  $\sigma > 18.0 \text{ M}\Omega \text{ cm}$  used in all of the experiments was purified with a Nanopure system. Silicon wafers were cut to a typical size of  $10 \times 20 \text{ mm}^2$  and were cleaned in piranha solution [1:3 (v/v)  $\text{H}_2\text{SO}_4/\text{H}_2\text{O}_2$ ], according to the usual procedure adapted in our laboratory.<sup>51</sup> (*Attention! Piranha solution is extremely dangerous and should be very carefully handled.*) Silicon wafers of the {100} orientation with one side polished (Semiconductor Processing Co.) were atomically smooth (microroughness within  $1 \times 1 \mu\text{m}^2$  surface area (here and everywhere) below 0.1 nm). After being cleaned, the substrates were rinsed thoroughly with Nanopure water and dried with dry nitrogen before LbL assembly.

**Fabrication and Release of LbL Films.** The LbL polymer films with a general formula (PAH–PSS)<sub>n</sub> ( $n = 2–17$ ) were fabricated using spin-assisted LbL assembly as adapted in our group and presented in details elsewhere.<sup>52–55</sup> Initially, a monolayer of PAH was deposited on a polymeric substrate from the 0.2% PAH solution by spin casting for 20 s. The substrate was then rinsed twice with Nanopure water and dried while spinning for 20 s. In the same manner, as the next step, a PSS monolayer was deposited from the 0.2% solution. This procedure was repeated until the needed number of polymer bilayers,  $n$ , was achieved.

The schematic of the deposition of sacrificial and underlying layers, which precedes the LbL deposition, is shown in Figure 2. For the preparation of LbL films to be released from a sacrificial substrate,<sup>56</sup> a PHS film was first spin cast on the freshly cleaned silicon substrate.<sup>57</sup> A droplet (200  $\mu\text{L}$ ) of the 5% PHS solution in dioxane was placed on the silicon substrate and rotated for 20 s at 6000 rpm. The thickness of the primary sacrificial PHS substrate deposited under these conditions was  $200 \pm 10 \text{ nm}$ . To vary the surface energy, additional sacrificial hydrophobic polymer layers (PVA, PS, and PMMA) were deposited on the primary PHS substrate from 5% solution in toluene at 6000 rpm (Figure 2). The thickness of the topmost PS, PVA, and PMMA films was in the range of 100–200 nm.

The fabrication and release of LbL films were performed in a Servicor-CPI Air laminar hood class 100. After fabrication, the LbL films were cut into approximately  $2 \times 2 \text{ mm}^2$  squares using a stainless steel microneedle and released by submersion in acetone, which dissolves the topmost and primary sacrificial layers. Then the LbL membranes were transferred to the surface of Nanopure water where they were picked up on various solid substrates for further study: a highly polished copper plate with a single micromachined hole,

a copper transmission electron microscopy (TEM) grid, and a clean silicon wafer.

**Characterization Methods.** AFM images were collected using a Dimension 3000 atomic force microscope (Digital Instruments) in light tapping mode according to the usual procedure adapted in our laboratory for ultrathin polymer films.<sup>58</sup> To evaluate the film thickness, the LbL film edge was scanned with AFM, and the images were analyzed with the bearing routine. TEM was performed with a JEOL 100CX-2 electron microscope at 100 kV. Bright-field optical images were captured with a Leica DM4000M optical fluorescence microscope. Contact angles were measured by using a Cam 101 contact angle meter (KSV). The thicknesses of the primary sacrificial PHS layer and underlying polymer layers were measured with an M2000U (Woolam) spectroscopic ellipsometer.

The buckling test was conducted for the evaluation of the elastic modulus of LbL films in accordance with the usual procedure.<sup>59,60</sup> As known, a uniform buckling pattern having a characteristic wavelength,  $\lambda$ , takes place when the thin film is subjected to a critical compressive stress. This wavelength is used to evaluate the elastic modulus in accordance with the usual routine.<sup>59</sup> To initiate the buckling pattern, a  $2 \times 2 \text{ mm}^2$  LbL membrane was placed on a poly(dimethylsiloxane) (PDMS) substrate, which was slowly compressed with a micrometer-sized increment. The total compressive distance was generally less than  $15 \mu\text{m}$ , keeping the compressive strain below 2%. The compression was monitored in a differential interference contrast (DIC) mode adjusted for maximum contrast. The images were analyzed by using Fourier transformation within ImageJ software.

## Results and Discussion

**Formation of Nanopores in the LbL Films on the PVA Surface.** To study the role of hydrophobic substrates in the morphology of the resulting LbL films, a truly flat polymer surface is required to eliminate the effect of surface irregularities and defects on the LbL deposition. The PHS primary sacrificial substrate and PVA topmost layer were chosen here as key model substrates for the LbL deposition. The PHS–PVA combination a possesses low microroughness of about 0.3 nm, which is well below that typically observed for a cellulose acetate substrate employed as a sacrificial layer.<sup>56</sup>

In this approach, we expected that the dewetting of poly-electrolyte solutions on hydrophobic PVA surfaces coupled with fast drying during spin casting would promote partial phase separation leading to the porous morphology of nanoscale LbL films. Indeed, it was found that during the spin-assisted deposition of the LbL film on the PVA layer the random network-like morphology is formed with a high concentration of nanopores reaching 30–40% (Figure 3a). This morphology is characterized by high microroughness reaching 4 nm within the  $1 \times 1 \mu\text{m}^2$  surface area, which is well above the microroughness of uniform LbL films, typically below 1 nm.<sup>61</sup> Phase images show high contrast indicating significant differences in material properties inside and outside of porous areas. All pores observed propagate through the entire thickness of the film. (See the discussion below.) The surface density of pores reaches  $10^{10} \text{ cm}^{-2}$ , which is about an order of magnitude higher than those known for track membranes<sup>62</sup> and microfiltration membranes prepared via ion beam aperture array lithography.<sup>63</sup> The overall film morphology

(51) Tsukruk, V. V.; Bliznyuk, V. N. *Langmuir* **1998**, *14*, 446.

(52) Zimnitsky, D.; Jiang, C.; Xu, J.; Lin, Z.; Zhang, L.; Tsukruk, V. V. *Langmuir* **2007**, *23*, 4509.

(53) Zimnitsky, D.; Jiang, C.; Xu, J.; Lin, Z.; Tsukruk, V. V. *Langmuir* **2007**, *23*, 10176.

(54) Jiang, C.; Markutsya, S.; Shulha, H.; Tsukruk, V. V. *Adv. Mater.* **2005**, *17*, 1669.

(55) Cho, J.; Char, K.; Hong, J.-D.; Lee, K.-B. *Adv. Mater.* **2001**, *13*, 1076.

(56) Mamedov, A. A.; Kotov, N. A. *Langmuir* **2000**, *16*, 5530.

(57) Watanabe, H.; Kunitake, T. *Adv. Mater.* **2007**, *19*, 909.

(58) Tsukruk, V. V. *Rubber Chem. Technol.* **1997**, *70*, 430.

(59) Nolte, A. J.; Rubner, M. F.; Cohen, R. E. *Macromolecules* **2005**, *38*, 5367.

(60) Jiang, C.; Singamaneni, S.; Merrick, E.; Tsukruk, V. V. *Nano Lett.* **2006**, *6*, 225.

(61) Tsukruk, V. V.; Rinderspacher, F.; Bliznyuk, V. N. *Langmuir* **1997**, *13*, 2171.

(62) Nuclepore membranes, [www.whatman.com/products/?pageID=Z7.57.291.22](http://www.whatman.com/products/?pageID=Z7.57.291.22).

(63) Han, K.; Xu, W.; Ruiz, A.; Ruckhoeft, P.; Chellam, S. *J. Membr. Sci.* **2005**, *249*, 193.

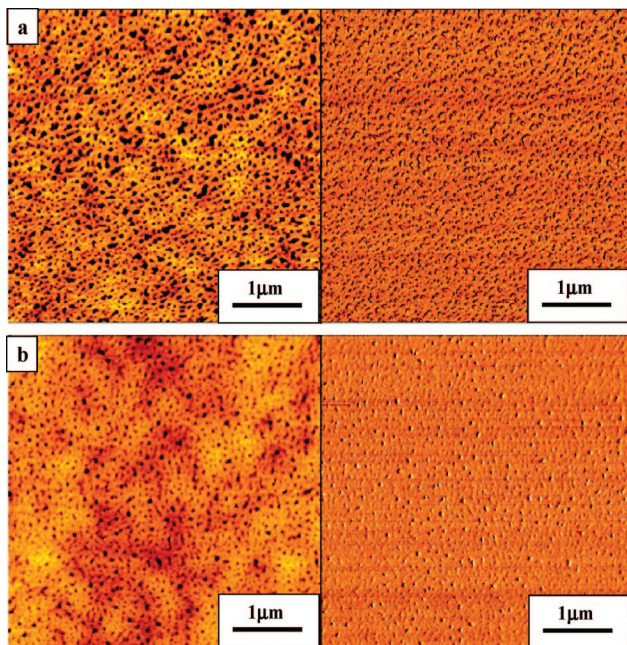


**Figure 3.** Large-scale AFM images of an LbL film composed of (a) 10 and (b) 15 PAH–PSS bilayers sitting on the PVA surface. The spinning speed is 6000 rpm. The left parts of the images represent the topography ( $z$  scale 30 nm), and the right parts represent the phase ( $z$  scale 40°).

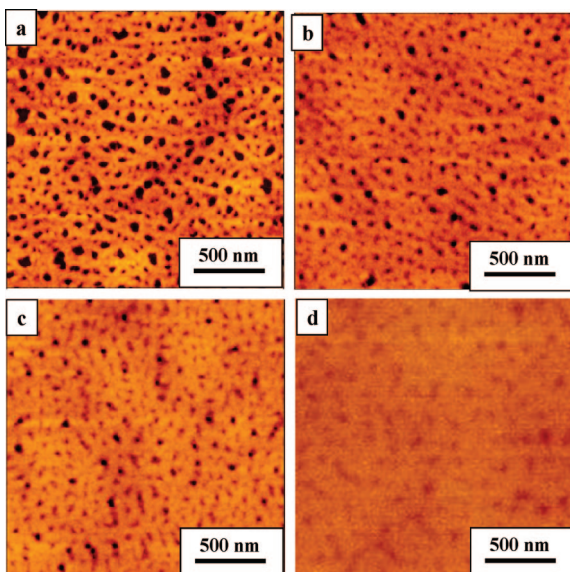


**Figure 4.** AFM images of LbL films composed of (a) 10, (b) 12, (c) 15, and (d) 17 PAH–PSS bilayers deposited on the PVA surface. The spinning speed is 6000 rpm, and the  $z$  scale is 30 nm.

is controlled by the number of polyelectrolyte bilayers with an obvious decrease in the pore concentration observed for thicker LbL films (Figure 3b).

Indeed, AFM images demonstrate that the addition of polymer bilayers caused a gradual decrease in both pore concentration and pore diameter, leading to the eventual disappearance of the highly contrasted network morphology for thick (PAH–PSS)<sub>17</sub> films (Figure 4). The diagrams of pore size distribution derived from AFM images confirmed this observation (Figure 5). The LbL film composed of 10 polymeric bilayers demonstrates a rather wide distribution of pore sizes with an average pore diameter of about 55 nm and the maximum pore size (cutoff size) reaching 80 nm. The increase in the number of polymeric bilayers leads

to smaller and more monodisperse nanopores (Figure 5). The LbL film composed of 15 polyelectrolyte bilayers showed small, monodisperse nanopores of  $25 \pm 8$  nm diameter with a cutoff size of 34 nm (Figure 5c). Concurrently, the film thickness increases with the number of polymeric bilayers from 16 nm for  $n = 10$  to 29 nm for  $n = 17$ . Nanopores in the (PAH–PSS)<sub>n</sub> film with 12 and 15 bilayers have nicely rounded shapes, whereas at 10 bilayers some larger pores are elongated. Presumably, for LbL films below 30 nm, several adjacent nanopores are merged and form larger and less regular pores.

The deposition of 17 bilayers leads to the healing of all nanopores and a continuous uniform LbL film surface with minor variation of the surface morphology (Figure 4d). The rms roughness gradually decreases with the increase in the number of polymer bilayers, reaching a value of 0.7 nm at 17 bilayers, which is a characteristic of uniform continuous LbL layers (Figure 5d). The fraction of nanopores in the overall surface area calculated from AFM images (underestimated because of the AFM tip smearing effect) also linearly decreases with the increase in the bilayer number (Figure 5d).

To elucidate these morphological changes, we carefully analyzed the pore dimensions from AFM cross-sectional analysis (Figure 6). As we observed, the depth of nanopores in films of 10 and 12 bilayers corresponded to the thicknesses of the film measured independently (16 and 20 nm, respectively), which indicates that the nanopores represent trough holes (i.e., the films are indeed perforated). In the case of 15 bilayers, the nanopore size is comparable to the diameter of the AFM tip (estimated to be close to 15 nm); as a result, the tip cannot reach the bottom of the hole. Nevertheless, the film composed of 15 bilayers is also perforated, which is shown by TEM. (See below.)

The dissolution of the underlying sacrificial substrate in acetone results in the release of the LbL film without affecting its surface morphology (Figure 7a). These floating films can be transferred onto TEM grids (Figure 7b). Most importantly, films consisting of as few as 10 bilayers were stable enough to preserve their integrity during release, handling, drying, and storing in the freely suspended state over openings for many months. Moreover, an independent testing of the mechanical properties revealed their mechanical strength. As was observed, a clear periodic wrinkle pattern appeared if the LbL film transferred onto an elastic substrate is subjected to compressive stresses (Figure 7c). This periodic pattern corresponds to the buckling instability and can be used to calculate the elastic modulus.<sup>59</sup> The elastic modulus of (PAH–PSS)<sub>10</sub> film with 30% porosity was estimated from wrinkle spacing as high as 2.1 GPa, which is on par with solid LbL films studied in the freely suspended state.<sup>34,64,65</sup> Considering that the elastic modulus of the uniform LbL film (PAH–PSS)<sub>17</sub> fabricated here is 3.3 GPa as determined from a similar buckling pattern (Figure 7d), we can conclude that the elastic modulus is close to that expected for the composite modulus of the porous film and thus the mechanical strength of the polyelectrolyte matrix is not compromised in the course of the formation of the nanoporous morphology.

In the released state, the complete morphology of the LbL membranes can be studied by scanning both sides of the film freely suspended over a TEM grid (compare parts a and b of Figure 8). The image of the top side is similar to that acquired by the direct scanning of the LbL film on the substrate (Figures 4c and 8a). This is an indication of the fact that the morphology of the films did not change during the dissolution of sacrificial

(64) Jiang, C.; Tsukruk, V. V. *Soft Matter* 2005, 1, 334.

(65) Markutsya, S.; Jiang, C.; Pikus, Y.; Tsukruk, V. V. *Adv. Funct. Mater.* 2005, 15, 771.

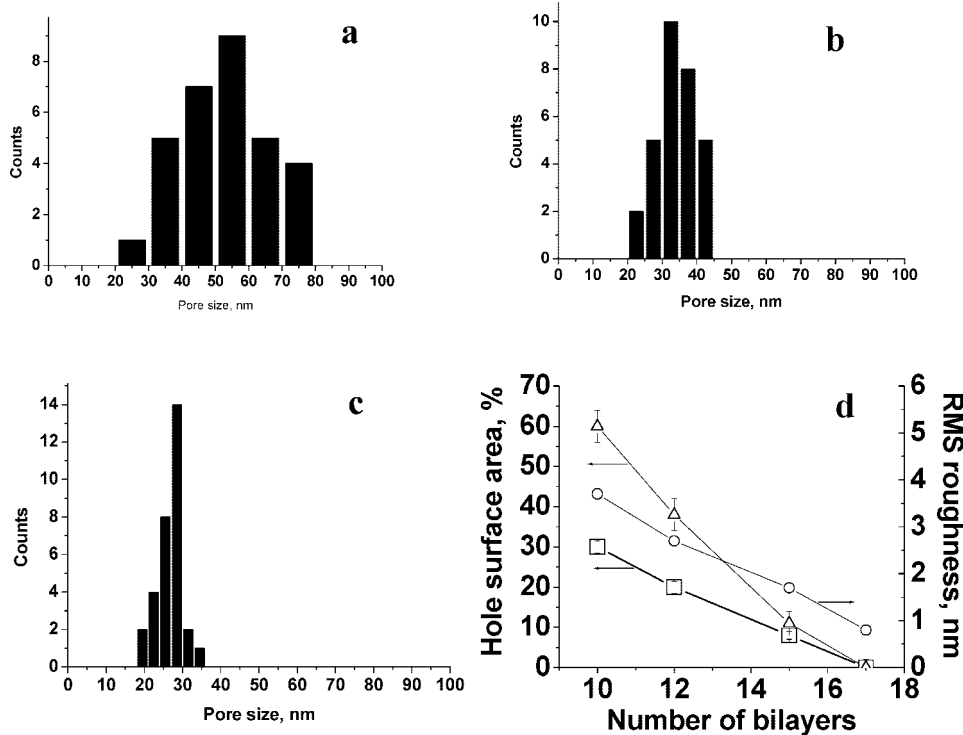


**Figure 5.** Diagrams of the pore size distribution of perforated LbL films comprising (a) 10, (b) 12, and (c) 15 polyelectrolyte bilayers derived from AFM data. (d) Dependence of the fraction of nanopore area and microroughness of the films upon the number of PAH–PSS bilayers. The nanopore fraction was calculated from AFM data ( $\square$ ) and derived from the values of the contact angle of the LbL film during deposition ( $\triangle$ ).

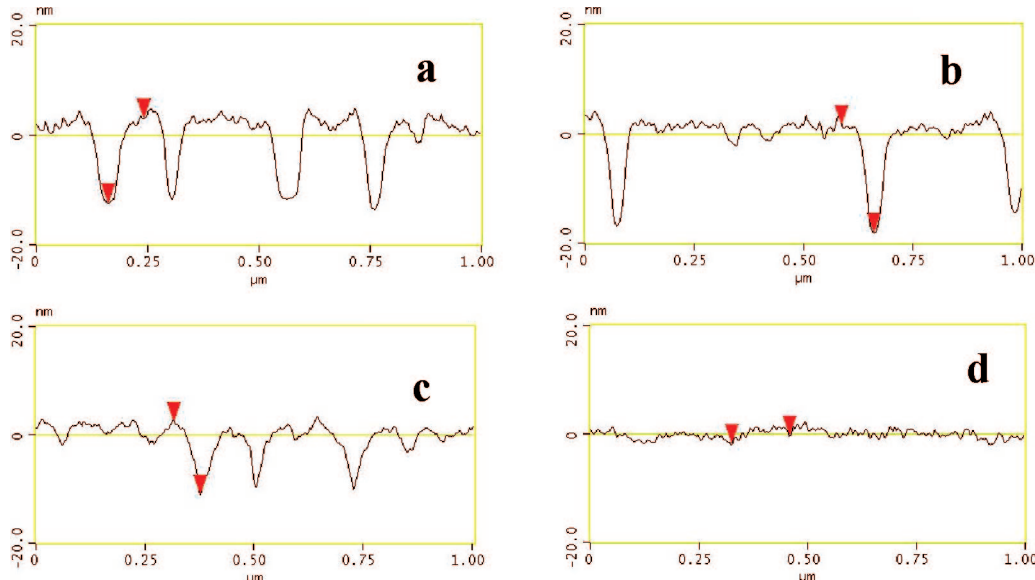


**Figure 6.** Cross-sectional analysis of  $1 \times 1 \mu\text{m}^2$  AFM images of LbL films composed of (a) 10, (b) 12, (c) 15, and (d) 17 PAH–PSS bilayers. The spinning speed is 6000 rpm, and the  $z$  scale is 40 nm.

layers and handling. The surface morphology of the bottom of the membrane that faced the underlying substrate is different from that for the top. The bottom side displays well-developed cellular morphology with cell dimension of 100–200 nm (Figure 8b). Nanoscopic through holes located in some of the cells are barely detectable with AFM (Figure 8b). The section analysis demonstrates conelike features (highlighted with dashed lines, well beyond tip dilation) as opposed to a rather smooth surface apart from holes on the “top” side (Figure 8, see cross-sections).

TEM images of the LbL membrane composed of 15 polymeric bilayers confirming the presence of the cellular-like morphology and the perforated nature of the film (Figure 9). Holes, which

correspond to the bright spots on the TEM image and are distributed throughout the membrane, have a perfectly round shape and are rather monodisperse in size. The average size of the nanopores appears to be larger in TEM images (40 nm) than in AFM images (25 nm) because of the tip dilation effect.<sup>66</sup> The spatial distribution of cells and their sizes and geometry are in agreement with the models of dewetting processes on surfaces due to confined 2D microphase separation known as Voronoi figures.<sup>67,68</sup> The geometrical parameters of such cellular-like

(66) Wong, Ch.; West, P. E.; Olson, K. S.; Mecartney, M. L.; Starostina, N. *JOM J. Miner. Met. Mater. Soc.* **2007**, 59, 12.

morphologies and the resulting surface morphologies and properties are controlled by the dewetting conditions and dynamics of solution spreading on surfaces, as will be discussed below for different substrates.

Considering the results on the surface morphologies of LbL films presented above, the general schematic of nanopore morphology evolution for the series of LbL films with an increasing number of bilayers can be presented in Figure 10. In this simplified schematic, initial porous LbL membranes are presented from a side view with conical through holes. Polyelectrolyte bilayers newly added to the top side of the LbL film resulted in decrease of opening size on this side. Apparently, at some point, which can be designated as critical thickness  $t_{\text{crit}}$  (corresponding to the critical number of bilayers,  $n_{\text{crit}}$ ), additional deposited layers decrease the pore size, leading to complete "healing" of the nanopores (Figure 10). Our data shows that smaller holes are healed completely after 15 bilayers whereas larger holes require several more bilayers to be completely closed.

**Additional Means to Control Nanoporous Morphology.** In the previous section, we demonstrated that the film morphology and nanopore size may be controlled by the number of PAH–PSS bilayers. Here, we briefly present two other means to control the nanoporous morphology: changes in the conditions for spin-assembly and selecting underlying surfaces with different wetting properties.

Figure 11 demonstrates the effect of spinning speed on the surface morphology and nanopore distribution (compare with Figure 4a). The increased spinning speed leads to higher shear forces affecting the chain conformation and reducing the thickness of the LbL films.<sup>69,70</sup> Indeed, the microroughness of the polyelectrolyte multilayers and the overall thickness of the films decrease with increasing spinning rate. As a result, the effect of nanopore healing occurs more quickly at a lower spinning rate, and thus it is advantageous to use a higher spinning rate for the preparation of perforated membranes. However, it should be noted that at this point we are able to tune film thickness and pore size independently only in the limited range of thickness discussed above. The alterations in the assembly process will be needed to control both of these parameters simultaneously over the wide ranges of thickness and pore diameter.

Alternatively, we utilized the surface property of the underlying substrate to control the formation of nanopore morphology in the LbL films. PS, PMMA, and PHS were chosen in addition to PVA because they differ in wettability (surface free energy) and possess very smooth surfaces with a microroughness below 0.3 nm.<sup>71</sup> As an alternative highly hydrophilic substrate, we selected the silicon dioxide surface of silicon wafers (Figure 12).

The effect of the underlying substrates on the LbL deposition has already been studied for many substrates, including unpolished silicon, glass, mica, and titanium foil.<sup>72,73</sup> However, in most cases prior to the deposition of polymer multilayers, the surfaces have been treated to achieve the proper surface charge.<sup>74</sup> Another alternative substrate was cellulose acetate, which was widely

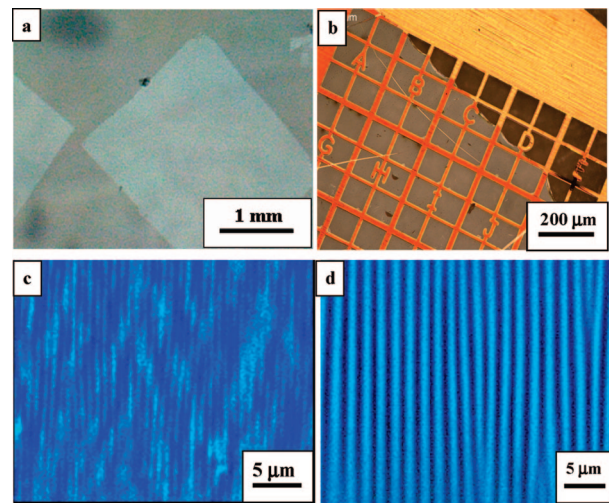


**Figure 7.** Optical images of a perforated (PAH–PSS)<sub>15</sub> membrane (a) floating on the water surface and (b) a membrane transferred onto the TEM grid and optical images of buckling instabilities for the (c) (PAH–PSS)<sub>10</sub> and (d) (PAH–PSS)<sub>17</sub> films.

used as a sacrificial material.<sup>33,34,37</sup> However, it was noticed that the contact angle of cellulose acetate changes significantly during the deposition of polyelectrolyte bilayers.<sup>54</sup> Therefore, we concluded that the heterogeneous morphology and the high roughness of cellulose acetate substrates (usually within 2–4 nm) affect the morphology of PAH–PSS films with a limited number of layers. Thus, this material was excluded from further consideration.

As clear from the AFM images, the silicon oxide layer becomes completely covered with a uniform LbL film (microroughness of 0.6 nm) with only two bilayers of PAH–PSS (four polyelectrolyte monolayers), in accordance with common knowledge.<sup>75</sup> Thus, no nanoporous morphology is observed under conventional deposition conditions (no post-treatment) on traditional, slightly charged, highly hydrophilic, and atomically smooth substrates even for the minimum number of LbL bilayers. In contrast, LbL films with several bilayers deposited on PMMA and PS surfaces still possess highly developed cellular morphology with a microroughness within 2–4 nm (Figure 12). The LbL film on the PHS surface showed intermediate morphology with somewhat reduced microroughness and weak network-like morphology (Figure 12b).

**Wettability on Different Hydrophobic Substrates.** As was shown above, the wettability of the surfaces may affect the morphology of LbL films to a great extent. An example of an interesting effect of surface wettability on the properties of LbL films has recently been demonstrated by the Kotov group.<sup>76</sup> Therefore, the evolution of the contact angle during LbL deposition on different hydrophobic substrates can provide interesting complementary information. First, we measured the value of the contact angle for all complete PSS–PAH LbL films and observed that it was independent on the underlying substrate and is equal to  $22 \pm 2^\circ$ . The measurements were conducted after the deposition of full bilayers with PSS as the topmost layer. In fact, the contact angle of the PAH–PSS films during LbL deposition on hydrophilic surfaces of mica, glass, silicon wafer, and titanium foil was demonstrated to become independent of

(67) *Spatial Tessellations: Concepts and Applications of Voronoi Diagrams*, 2nd ed.; Okabe, A., Boots, B., Sugihara, K., Chiu, S. N., Eds.; John Wiley & Sons: New York, 2000.

(68) Ogawa, H.; Kanaya, T.; Nishida, K.; Matsuba, G. *Eur. Phys. J. Special Top.* **2007**, 141, 189.

(69) Lefaux, C. J.; Zimnitsky, A. V.; Dobrynin, A. V.; Mather, P. T. *J. Polym. Sci., Part B: Polym. Phys.* **2004**, 42, 3654.

(70) Patel, P. A.; Dobrynin, A. V.; Mather, P. T. *Langmuir* **2007**, 23, 12589.

(71) Sperling, L. H., *Introduction to Physical Polymer Science*; John Wiley & Sons: New York, 2001.

(72) Kolasinska, M.; Warszynski, P. *Bioelectrochemistry* **2005**, 66, 65.

(73) Kolasinska, M.; Warszynski, P. *Appl. Surf. Sci.* **2005**, 252, 759.

(74) Tang, Z.; Wang, Y.; Podsiadlo, P.; Kotov, N. A. *Adv. Mater.* **2006**, 18, 3203.

(75) Tsukruk, V. V.; Bliznyuk, V. N.; Visser, D. *Macromolecules* **1997**, 30, 6615.

(76) Shim, B. S.; Podsiadlo, P.; Lilly, D. G.; Agarwal, A.; Lee, J.; Tang, Z.; Ho, S.; Ingle, P.; Paterson, D.; Lu, W.; Kotov, N. A. *Nano Lett.* **2007**, 7, 3266.

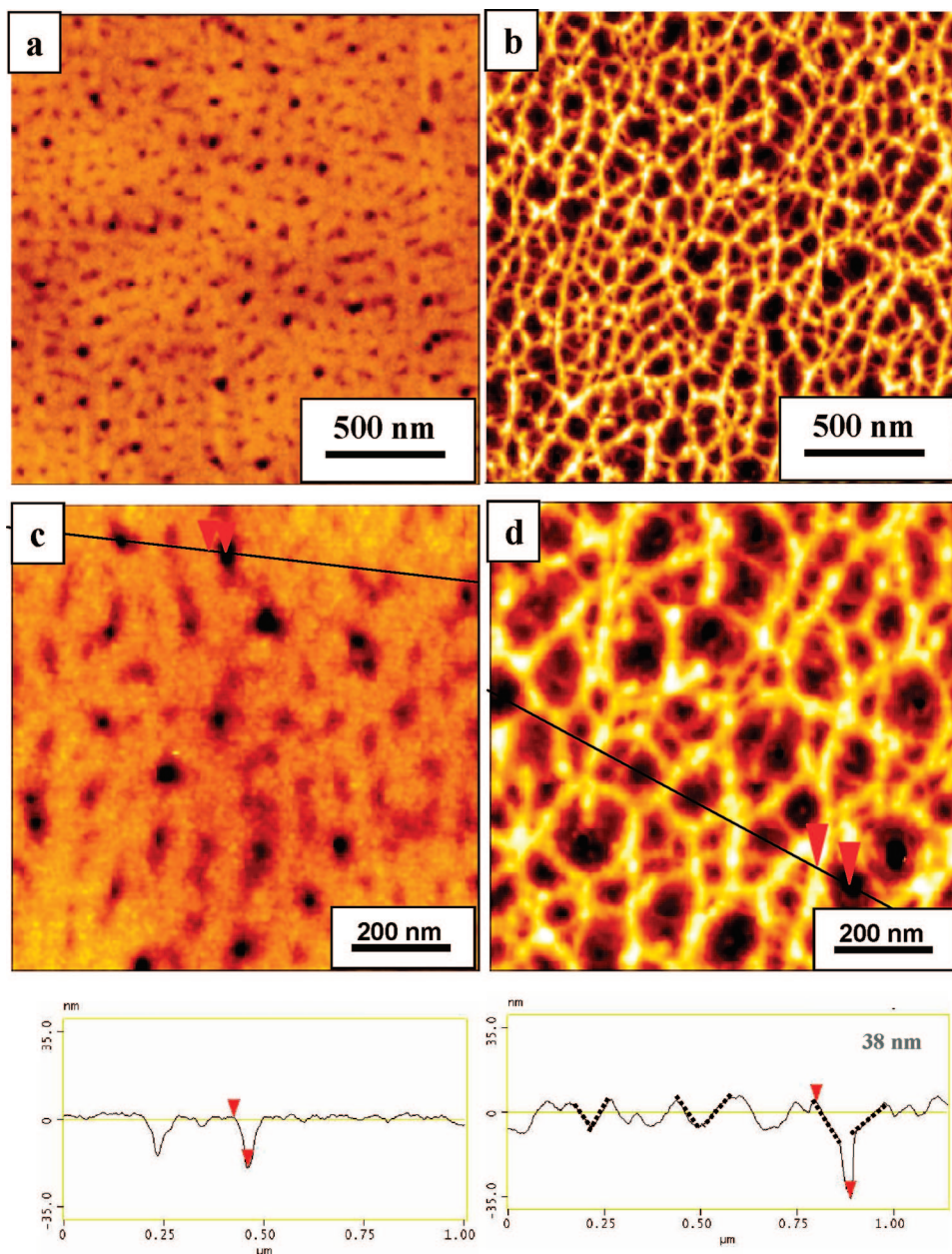


**Figure 8.** AFM images at different magnifications and cross-sections of the (a, c) top and (b, d) bottom sides of the freely suspended (PAH–PSS)<sub>15</sub> membrane transferred onto the TEM grid.

the substrate nature after the deposition of two to three bilayers.<sup>77</sup> These results are also consistent with previously reported data for the spin-assisted deposition of PAH–PSS films on the sacrificial cellulose acetate layer.<sup>78,79</sup> Without the addition of salt, the contact angle of the polyelectrolyte PAH–PSS pair was measured to be within the range of 20–25°, with no distinct difference between a PAH and a PSS exterior.<sup>77,80</sup>

Our observation indicated that depositing just two PAH–PSS bilayers on freshly prepared silicon oxide increases the contact angle to 22° (from about 10° for a freshly prepared silicon wafer), thus confirming the full uniform coverage under the given preparation conditions (Figures 12 and 13). For hydrophobic substrates, the contact angle eventually drops from 60–95° to 22°; however, a different number of bilayers is required to

complete this conversion and to reach a plateau at  $22 \pm 2^\circ$ , which is a typical value for the PAH–PSS film (Figure 13).<sup>77</sup> In the case of PHS, PMMA, and PS, up to eight PAH–PSS bilayers are required to achieve complete surface coverage of the LbL film and heal the original pores ( $n_{\text{crit}}$  is within 4–8) (Figures 10 and 13). In the case of the PVA substrate, LbL films preserved a perforated morphology until reaching a thickness of about 25 nm ( $n_{\text{crit}} = 17$ ), which is a very high value as compared to that for other surfaces. For all substrates, (PAH–PSS)<sub>n</sub> films with  $n > n_{\text{crit}}$  are complete, smooth, and homogeneous, as is independently verified by AFM.

To understand these results, the wettability of the underlying polymer substrates employed here has to be discussed in terms of the surface free energy and the spreading behavior of the sacrificial substrates (Figure 14).<sup>81,82</sup> As is known, the spreading coefficient that is utilized to characterize the wetting–dewetting

(77) Cho, J.; Char, K. *Langmuir* **2004**, *20*, 4011.

(78) Jiang, C.; Markutsya, S.; Tsukruk, V. V. *Adv. Mater.* **2004**, *16*, 157.

(79) Jiang, C.; Tsukruk, V. V. *Adv. Mater.* **2006**, *18*, 829.

(80) Chen, W.; McCarthy, T. J. *Macromolecules* **1997**, *30*, 78.

(81) Choi, S.-H.; Newby, B.-M. Z. *Langmuir* **2003**, *19*, 1419.

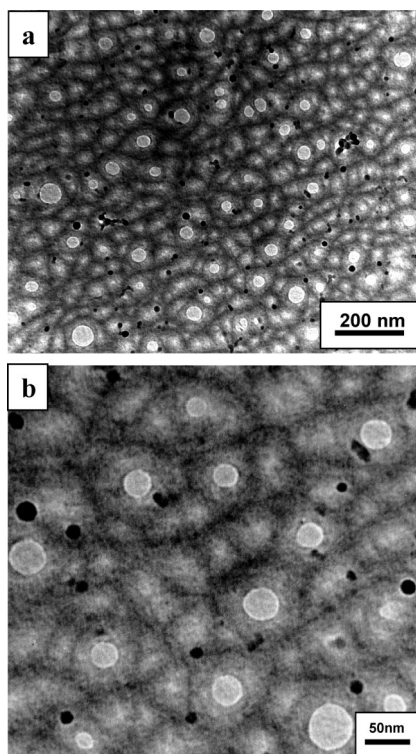


**Figure 9.** TEM images of a perforated, freely suspended  $(\text{PAH}-\text{PSS})_{15}$  membrane at different magnifications.

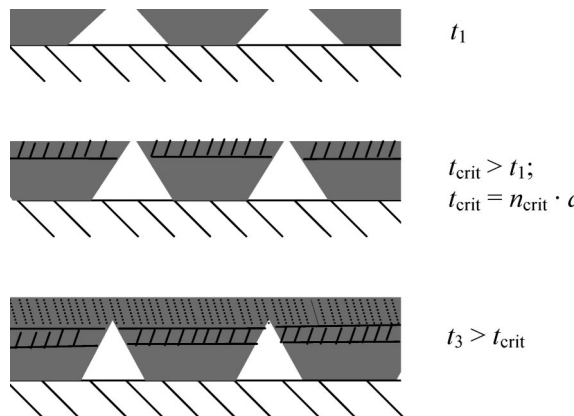


**Figure 10.** General schematic of the evolution of nanopore morphology with an increasing number of bilayers.

behavior is directly related to the difference in free energy of the material in contact, with a contribution from the interfacial free energy.<sup>71</sup> If the molecules of the materials deposited have a stronger affinity to the solid surface than to each other (the adhesive forces are stronger than the cohesive forces), then surface wetting occurs. When the interactions between molecules and the surface are unfavorable, dewetting takes place. Dewetting of polyelectrolytes on hydrophobic surfaces should lead to non-uniform deposition with the formation of cellular-like patterns and holes within LbL films with a limited number of bilayers.

Considering our materials from the point of view of spreading behavior, we should note that both polyelectrolytes (PAH and PSS) possess high surface energies, 56 and 58  $\text{mJ/m}^2$ , respectively.<sup>83</sup> These values are much higher than the free energies for our hydrophobic substrates (decreasing from

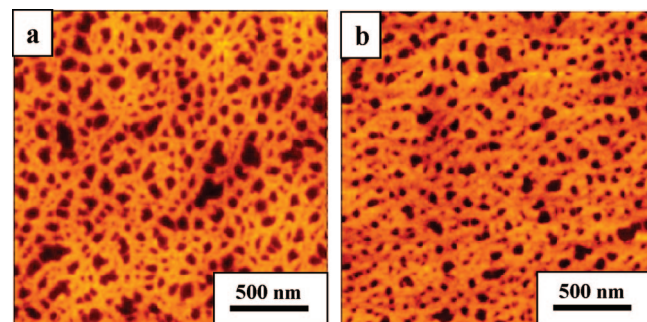


**Figure 11.** AFM images of an LbL film composed of 10 bilayers deposited on a PVA substrate. The spinning speed (a) is 8000 and (b) 4000 rpm, and the  $z$  scale is 30 nm.

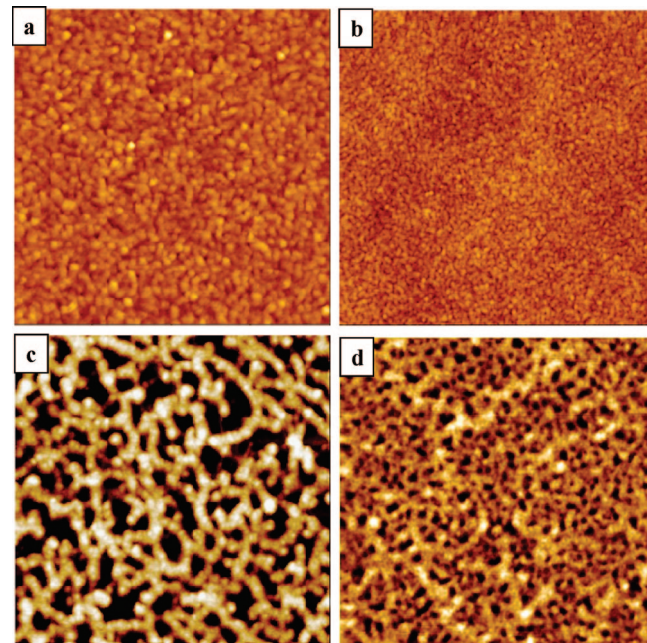


**Figure 12.** AFM images of LbL films composed of (a, b) 2 and (c, d) 6 bilayers deposited on the (a) silicon, (b) PHS, (c) PMMA and (d) PS surfaces. The  $z$  scale is 20 nm.

41.8  $\text{mJ/m}^2$  for PHS to 36.5  $\text{mJ/m}^2$  for PVA) but much lower than for the hydrophilic silicon oxide surface ( $72 \text{ mJ/m}^2$ ).<sup>84,85</sup> Considering minor contributions from the interfacial free energy, these large differences (of opposite sign) immediately indicate that spreading behavior will be highly favorable on a silicon oxide surface but dewetting will be favorable on all hydrophobic substrates. Moreover, we can rank substrates utilized here in accordance with their free-energy difference of between 57  $\text{mJ/m}^2$  for polyelectrolyte material and those for hydrophobic substrates and compare them with each other (Figure 14). Adding a plot of the number of layers required to form a homogeneous LbL film,  $2n_{\text{crit}}$ , immediately shows a strong correlation between these parameters. For surfaces with a negative difference (complete wetting predicted, silicon oxide), the initial four polyelectrolyte layers (two bilayers) form a homogeneous film. Further increases in the free-energy difference to 15.2 (PHS), 15.9 (PMMA), 16.3 (PS), and finally 20.5  $\text{mJ/m}^2$  (PVA) are accompanied by a corresponding increase in the number of

(83) Mhamdi, L.; Picart, C.; Lagneau, C.; Othmane, A.; Grosgogeat, B.; Jaffrezic-Renault, N.; Ponsonnet, L. *Mater. Sci. Eng., C* **2006**, *26*, 273.

(84) Lin, H.-C.; Wang, C.-F.; Kuo, S.-W.; Tung, P.-H.; Huang, C.-F.; Lin, C.-H.; Chang, F.-C. *J. Phys. Chem. B* **2007**, *111*, 3404.

(85) Zisman, W. A. *ACS Adv. Chem. Ser.* **1964**, *43*, 1.

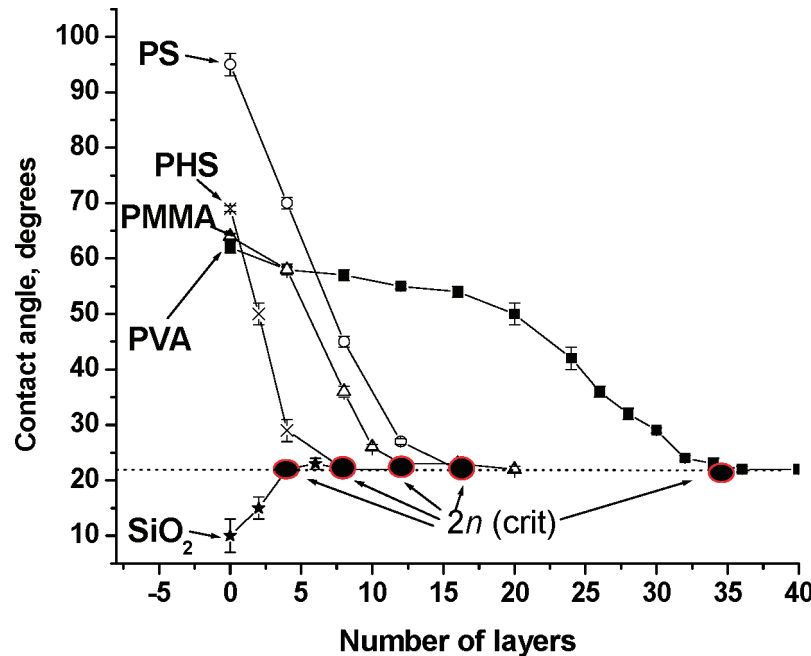


**Figure 13.** Dependence of the contact angle of LbL films on the number of polyelectrolyte layers on various substrates. The dotted line shows the contact angle for the complete LbL film ( $22^\circ$ ).

polyelectrolyte layers required to heal the initial dewetted cellular pattern from 8 to 34 (Figure 14). In the case of the substrate with the highest difference in the surface free energy, PVA, strong dewetting leads to the preservation of the perforated structure even for thicker LbL films (>20 nm). These LbL films with perforated morphologies are robust enough to sustain the freely suspended state, a property utilized to fabricate perforated freely suspended membranes.

The data collected here can also be used to calculate the porosity of the LbL films by applying Cassie's law to composite surfaces.<sup>86</sup> As known, the contact angle of a liquid on a composite surface,  $\theta_c$ , is defined by the area fraction of components  $\gamma_1$  and  $(1 - \gamma_1)$  and their individual contact angles  $\theta_1$  and  $\theta_2$ :  $\cos \theta_c = \gamma_1 \cos \theta_1 + (1 - \gamma_1)\cos \theta_2$ . The validity of this approach was confirmed for smooth surfaces with nanoscale thicknesses of the composite layers.<sup>87</sup> From the measured contact angles of the LbL film and individual contact angles of PVA ( $62^\circ$ ) and the polyelectrolyte film ( $22^\circ$ ), we derived the area fraction of nanopores for various numbers of LbL bilayers (Figure 5d). Surprisingly, the fraction of nanopores derived from these calculations was very high, reaching 60% for PAH–PSS films with 10 bilayers. The discrepancy in the AFM data can be related to the presence of small (5–10 nm) nanopores, which cannot be detected by AFM because of the tip dilation effect. It is worth noting that for the LbL film with 15 bilayers the porosity obtained from two different methods virtually coincides, which confirms the disappearance of smaller nanopores because of their preferential healing.

### Conclusions

We demonstrated ultrathin (thickness down to 20 nm) perforated LbL membranes with tunable nanopore sizes in the range of 20–50 nm using spin-assisted LbL assembly on hydrophobic sacrificial polymeric substrates. The size of the nanopores might be controlled by changing the number of

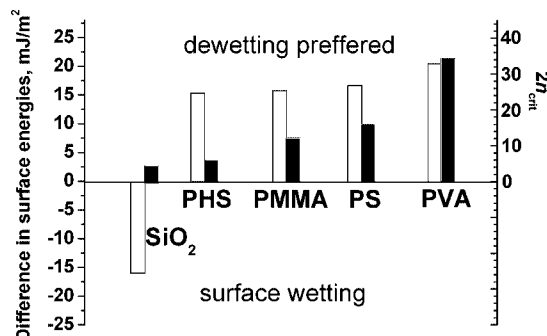


**Figure 14.** Critical number of polyelectrolyte monolayers (filled columns) vs the difference in surface free energy between polyelectrolytes and the underlying hydrophobic substrates (open columns).

polyelectrolyte bilayers in the LbL film and the speed of spinning during LbL assembly and by the choice of the proper hydrophobic substrates. The formation of nanopore morphology is caused by the poor wettability of hydrophobic substrates by the polyelectrolytes. The effect of underlying unfavorable (noncharged and nonhydrophilic) surfaces on LbL deposition is well known; however, these hydrophobic surfaces have never been used for constructive purposes. This is a counterintuitive strategy because the traditional purpose of the surface studies is to eliminate the substrate effect (usually extended to the initial two to five bilayers) and obtain uniform LbL multilayers.

In contrast, the dewetting of the initial few polyelectrolyte layers on hydrophobic substrates with various free energies is utilized here for the controlled fabrication of freely suspended perforated membranes with a narrow pore size distribution and nanoscale thickness. We suggest that contrary to the common fact that smooth hydrophilic and charged substrates with high surface energy are preferable for the fabrication of homogeneous LbL films, hydrophobic surfaces with low surface energy provide the best opportunity for the fabrication of perforated nanoscale membranes with unique nanoporous morphology. In general, using substrates with lower surface energy may provide thicker and stronger freely suspended LbL membranes with the

(86) Cassie, A. B. D.; Baxter, S. *Trans. Faraday Soc.* **1944**, *40*, 546.

(87) Luzinov, I.; Julthongipit, D.; Malz, H.; Piontek, J.; Tsukruk, V. V. *Macromolecules* **2000**, *33*, 1043.

preservation of the truly perforated structure. However, hydrophobic substrates may be used for the preparation of perforated, freely suspended LbL membranes only under conditions of their near-molecular smoothness combined with easy dissolution in selective solvents not affecting the LbL films during their release.

We suggest that the nanoscale thickness of perforated membranes provides an excellent prospective for much higher transport rates through these membranes during separation. High porosity and easy chemical functionalization of the selected side is a signature of these LbL membranes. The potential applications of such perforated nanomembranes with properly modified surfaces include the efficient separation of large biomolecules, nanoparticles, carbon nanotubes, and quantum dots with high

selectivity. Moreover, suspending these perforated LbL membranes over microfabricated microscopic hole arrays in a manner similar to that employed for microthermal imagers<sup>88</sup> can lead to the fabrication of intriguing sieve arrays with hierarchical multiscale micro- and nanoporous structures.

**Acknowledgment.** This work was supported by AFOSR, FA9550-05-1-0209, and NSF-CBET-0506832 grants. We thank Dr. E. Kharlampieva and K. Bergman for technical assistance and discussions.

LA7038575

---

(88) Jiang, C.; McConney, M. E.; Singamaneni, S.; Merrick, E.; Chen, Y.; Zhao, J.; Zhang, L.; Tsukruk, V. V. *Chem. Mater.* **2006**, *18*, 2632.